Acta Materialia 216 (2021) 117139

Contents lists available at ScienceDirect

Acta Materialia

journal homepage: www.elsevier.com/locate/actamat

Full length article

Can Y_2O_3-MgO eutectics be new promising structural and optical ceramics?

Bibi Malmal Moshtaghioun[a,b,*], Jose I. Peña[a], Rosa I. Merino[a,*]

[a] Instituto de Nanociencia y Materiales de Aragón, CSIC-Universidad de Zaragoza, 50009 Zaragoza, Spain
[b] Departamento de Física de la Materia Condensada, Universidad de Sevilla, PO Box 1065, 41080 Sevilla, Spain

ARTICLE INFO

Article history:
Received 30 November 2020
Revised 21 June 2021
Accepted 26 June 2021
Available online 1 July 2021

Keywords:
Y_2O_3-MgO eutectic
Composite
Laser floating zone
Infrared transmission

ABSTRACT

The manuscript addresses the solidification of Y_2O_3-MgO eutectic composites for the first time, and the study of their microstructure, mechanical properties and infrared transmittance. The composites with eutectic composition (20 % vol MgO) have been solidified using the laser floating zone method, at solidification rates between 25 mm/h and 750 mm/h. Their microstructure has been quantified and the conditions for coupled or cellular regime determined. They are dense, with elastic modulus, as determined from nanoindentation tests of around 200 GPa. The highest 3-point flexural strength (256±25 MPa) values and highest infrared optical transmittance has been observed for the material solidified with the finest, still homogeneous microstructure that could be achieved. This microstructure, which is achieved at a solidification rate of 50mm/h, consists of MgO fibers of 600 nm diameter embedded in the Y_2O_3 matrix. The thin MgO rods and the associated residual stress field contribute to the material strength as they deviate the propagating crack. The Vickers Hardness ranged from 9.5 to 11.5 GPa, with mild increase with the decrease of the microstructural size which has been rationalized as the MgO rods blocking the movement of dislocations in the matrix, as in other studied composites. Indentation fracture toughness values around 3 MPa.$m^{1/2}$, independent of the sample microstructure, have been measured. In the longitudinal direction transmittance values higher than 80 % in the wavelength range from 3.5 to 7 μm, for 1 mm thick slices have been measured. Light scattering limits the short wavelength cut-off to around 2 μm for light travelling in the longitudinal direction, while a transmittance gap is observed in the transverse direction, of photonic crystal like nature.

1. Introduction

Optical ceramics need to meet certain criteria for application in infrared (IR) systems. These ceramics should have combination of properties such as high transparency and excellent mechanical properties, increased thermal shock resistance and lower emissivity, simultaneously. Among the commonly available and durable mid-infrared materials, both polycrystalline Y_2O_3 and MgO are infrared transparent, have a longer wavelength cutoff and lower emissivity than other mid-infrared materials, but their unsatisfactory mechanical properties restrict their applications. To obtain high infrared transmittance, a requirement for low optical scatter in a composite material is that grain size must be substantially smaller than the wavelength of light to reduce optical scatter to tolerable levels. The MgO–Y_2O_3 composite (M:Y, usually ~50 vol % MgO) has attracted recent attention. It represents a new class of oxide/oxide optical nano-composite by combining two optically excellent mid-wave infrared transmitting materials. So, Y_2O_3–MgO nano-composite tend to exhibit a combination of IR optical and mechanical properties superior to those of single-phase optical ceramics due to the fact that the presence of one phase naturally impedes the grain growth of the adjacent phases [1,2].

The fabrication of fully dense nano-composites with fine grains, homogenous microstructures and uniform phase distribution is particularly challenging because of the need to control the microstructural size of both components. To approach these characteristics, several attempts with different techniques were tried that are listed in Table 1. Wang et al [3] attained MIR transmittance up to 80% in 0.9 mm thick fully dense samples fabricated by traditional ceramic consolidation techniques. These composites had 310 nm grain size and an enhanced hardness of 10.6 GPa. Harris et al. [4] and Xie et al. [5] improved the properties using the traditional sintering method followed by hot isostatic pressing. In this case, up to 83% MIR transmittance in the wavelength range between 2.5

* Corresponding authors.
E-mail addresses: mali_moshtagh@us.es, mali@unizar.es (B.M. Moshtaghioun), rmerino@unizar.es (R.I. Merino).

https://doi.org/10.1016/j.actamat.2021.117139

Table 1
Powder details, sintering parameters, characteristics of sintered Y_2O_3-MgO nanocomposites from the literature. All the listed composites were prepared with 50/50 volume ratio and starting with nanopowders. Accronyms used in the table: TD: theoretical density; CIP: cold isostatic pressing; PlS: pressureless sintering; VacS: vacuum sintering; HP: hot pressing; HIP: hot isostatic pressing; SPS: spark plasma sintering; LFZ: laser floating zone solidification; ANN: post sinter annealing; *HV*: Vickers Hardness: E = Elastic Modulus; σ_f: 3 point bending strength; IFT; indentation fracture toughness.

Starting powder size	Ceramic processing conditions (sequential)	Final density and average grain size	Mechanical properties	IR transmittance /wavelength range / sample thickness	Note
~15nm	PlS at 1400°C for 2 h, HIP 1350 C for 1 h and ANN at 1000 °C (10 h)	99.5%, 310 nm	*HV0.3* =10.6 GPa	62%-80% / 3-7 μm / 0.9 mm thick	Wang 2010 [3]
~30nm	CIP to >60 % TD; VacS in graphite furnace to >96% TD; HIP; ANN at 1100 °C (20h)	99.9%, 150 nm	*HV0.2-0.3* =11.4 GPa, E = 230 GPa.	80% / 4-6 μm / near to 3.00 mm thick	Harris 2013 [4]
~17nm	CIP at 210 MPa to >50% TD; PlS at 1400°C (2h); HIP at 1350°C (1h) at 200 MPa; ANN at 1000 °C (15h).	Fully dense, ~180 nm	-	83% / 2.5–6 μm / 1.00 mm thick	Xie. 2017 [5]
~13nm	HP at 1200°C and 50MPa (1h); ANN at 1000°C (15 h)	97.3%, ~100 nm	-	75% / 5 μm / 0.5 mm thick	Xu 2015 [6]
12-20nm	HP at 1300°C and 40MPa (1h); ANN at 1000°C (21h)	Fully dense, ~110 nm	*HV2* =10.59 GPa: *IFT* = 1.58-2.55 MPa $m^{1/2}$; σ_f = 258-310 MPa.	84.9% / 5.3 μm / 0.75 mm thick	Ma 2017 [7]
13nm	SPS at 1100 °C and 50MPa (5 min); ANN at 1000 °C (15h).	Fully dense, ~100 nm	-	57%/ 5 μm / 1.22 mm thick	Xu 2015 [8]
60nm	SPS at 1200 °C and 80MPa (3 min); ANN at 1000 °C (15h).	Fully dense, ~90 nm	-	80% / 1.8 - 6.4 μm / 1mm thick	Jiang 2010 [9]
20nm	SPS at 1150 °C and 70MPa (10min); ANN at 1100 °C (5h).	99%, ~170 nm	*HV1* =10.2 GPa	80.9% / 5 μm / of 1.5mm thick	Permin 2020 [10]
50nm	SPS at 1250 °C and 70MPa (10 min); ANN at 1000 °C (10h).	99.4%, ~142 nm	*HV0.2* =11.9 GPa, *IFT* = 2-2.26 MPa $m^{1/2}$, E = 241 GPa.	78%-84.3% / 2.5-6.5 μm /1 mm thick	Liu 2021 [11]
20 vol % MgO	LFZ (directional solidification), 50 mm/h pulling rate	Full density, ~ 1.3 μm.	*HV1* = 10.2 GPa; *IFT* = 3.0 MPa $m^{1/2}$; E = 213 GPa; σ_f = 256 MPa	~90 % (along) and ~70 % (across)/ 6 μm / 1mm thick	This work (see text)

and 6 μm in a 1.0 mm thick fully dense composite with smaller grain size (below 200 nm) and hardness of 11.4 GPa was obtained [5]. Also using hot-pressing techniques, ceramics with still smaller grain sizes were obtained by others [6, 7], and in the optimal case transmittance up to 84.9 % for 1 mm thick annealed nanocomposites with grain size of about 110 nm was observed and hardness of 10.59 GPa was achieved [7]. More recently, there were several studies with modern techniques of sintering like spark plasma sintering (SPS). Mild improvement in the results for annealed fully-dense composites were obtained [8-11]. In general, the transmittance of SPS as processed samples was quite low, that increased after annealing in air, probably due to recovery of the oxygen stoichiometry. Transmittance values above 80% for 1.0 mm thick samples was obtained by post-SPS annealing of Y_2O_3-MgO with different composition ratios, with the highest value for the 50/50 vol% due to its smallest grain size of 142 nm, and showing hardness of 11.9 GPa [11].

Up to now, research has been mainly focused on optimization of the sintering conditions of Y_2O_3– MgO nano-composites with a composition of 50/50 vol% to achieve reduced grain size with theoretical density which resulted in improved optical and mechanical properties. However, no report can be found for the Y_2O_3–MgO composite in the eutectic point (80/20 vol%) which has lower melting temperature (2110 °C) [12] compared with a composition 50/50 vol% (~2400 °C) and consequently the fully dense ceramics can be fabricated from melt-grown techniques. The laser floating zone (LFZ) method is suitable to this purpose since it provides a good control over the shape of the solidification front, that determines the microstructure of grown eutectic ceramics and it is a powerful means to get fine and homogeneous microstructure [13, 14].

Surprisingly, there is no report in the literature of the fabrication of this eutectic ceramic. So, it raises various questions of great interest, namely: Can Y_2O_3– MgO eutectic ceramics be fabricated by LFZ? If so, how does LFZ processing impact the optical and mechanical properties? Is it comparable or better than those fabricated with other techniques used before with the nominal composition of 50/50 vol%? In the present study, we will try to answer these questions with the aim of providing more efficient means for fabrication of Y_2O_3– MgO composite with optimal characteristics.

2. Experimental procedure

The starting materials were commercially available Y_2O_3 powder (Sigma-Aldrich, 99.99%) and MgO powder (Sigma-Aldrich, >99%). MgO powder was dried in a furnace at 1200 °C for 6 h to remove the possible moisture absorption from outside air [15]. The eutectic composition between Y_2O_3 and MgO appears at 50 mol% Y_2O_3 and 50 mol% MgO (80:20 vol%) and its melting temperature is around 2110 °C [12]. The eutectic composition was mixed and homogenized with polyvinyl alcohol in an agate mortar for 10 min. Feedstock rods of ~ 2.6 mm in diameter and up to 5 cm in length were prepared by cold isostatic pressing for 5 min at 200 MPa followed by sintering in a furnace at 1500 °C for 12 h. The materials were then grown by directional solidification from the melt using the laser-heated floating zone (LFZ) method with a CO_2 laser in air [16]. The procedure is initiated by forming a melt drop on the end of a sintered rod (feedstock) by heating with a anular-shaped CO_2-laser beam. Another sintered rod is pushed into this the molten volume until it forms a stable molten volume between both solid pieces. The molten volume of material is held between the solidifying crystal and the feed rod, and fed on one side by the feed rod while the solidified rod is pulled from the other side. To eliminate feedstock porosity and decrease its diameter, two solidification steps with feed rate of 200 mm/h and growing crystal pulling rate of 300 mm/h were first performed. On these steps, feed and growing rods were counter-rotated at 50 rpm. In the third and last solidification step, the feed and grown rods were moved at

the same rate (no diameter reduction) using a variable growth rate between 25 and 750 mm/h to evaluate its effect on the microstructure, optical and mechanical properties of the resulting Y_2O_3– MgO eutectic ceramics. A nominal laser output power of 60-70W has been used in the last step to maintain a constant feed and very small molten zone. This step was performed under two different rotation conditions: counter rotating the solidified rod and the feed rod at 50 rpm and without rotation. Finally, eutectic rods of ~1.6 mm were fabricated.

The grown eutectic rods were cut, ground and polished to a 0.25 μm finish. Additionally, all were characterized microstructurally by a field emission scanning microscope (FE-SEM) (Merlin, Carl Zeiss, Germany) with an EDS microanalysis system (INCA350, Oxford Instruments, United Kingdom). Microstructure observations were done from both transverse sections using the back-scattered emission (BSE) mode on carbon coated-polished surfaces. The phase interspacing, λ, was determined from the transverse cross-section SEM micrographs. The microstructural feature size (transverse phase size and intespacing) has been determined as the arithmetic mean of 40 measurements for each Y_2O_3-MgO eutectic ceramics grown at different rates, taken on SEM micrographs by use of Software Image J. The given error bar is the standard deviation calculated from the total number of measurements per specimen. The transverse size has been determined from equivalent rod diameter in equiaxial MgO sections (circular, triangular sections or cell boundaries), or from <width+length>/2 in lamellar areas.

X-ray diffraction (XRD) diagrams were registered on a RIGAKU diffractometer, model Ru300 (Rigaku Corporation) equipped with Cu rotating anode, a graphite monochromator to select the Cu-Kα radiation and working at 40 kV and 80 mA. We performed 2θ scans between 15° and 90°, with 0.03° steps and 3s or 1s per step. The samples were placed as solidified on the diffractometer, with the solidification axis normal to the diffraction plane, that is, only the crystallographic planes lying perpendicular to the pulling direction (growth axis) will give rise to diffraction peaks.

Infrared transmission spectra were measured at wavelengths shorter than 2.5 μm with a UV-Vis-NIR spectrometer (Cary 5000, Agilent Technologies Inc., USA) and in the range, from 2.5 to 10 μm, with a mid-infrared (MIR) spectrophotometer (Spectrum 100 FTIR, Perkin-Elmer Inc., USA). The sample slices to be measured were ground to near to 1mm thickness and then both faces polished to 0.25 μm finish. The sample thickness was measured with a digital caliper with ±0.02 mm accuracy. A diaphragm of 0.5 mm diameter was used to select the central area of the sample to measure transmittance.

Furthermore, mechanical properties were studied by Vickers-indentation tests (Matsuzawa MXT70 micro-hardness tester, from MATSUZAWA SEIKI CO., LTD, Tokyo, Japan) applying a load ***(P)*** of 9.81 N for 15 s on cross-sections of eutectic rods (10 indentations per specimen, five on transversal and five on longitudinal cross section) to evaluate Vickers hardness and indentation fracture toughness [17,18]. The room-temperature micro-hardness was then calculated from the average length of the two diagonals *(d)* of the residual impressions and load of *P* [17,18] as:

$$H_v = \frac{2P\sin(136^\circ/2)}{d^2} \cong 1.854\frac{P}{d^2} \quad (1)$$

The same indentations were further used to measure the indentation fracture toughness. As the ratio of the c_p/a_p, where a_p is the half diagonal length of the print and c_p is the distance between the centre of the print to the end of the crack, is close to 2.5, the Median type expression was used with the Anstis equation [19], $K_{IC} = 0.016\,(E/H)^{1/2}P/{c_p}^{3/2}$, *P* is load, *H* is the Vickers hardness and *E* is the Young modulus obtained from nanoindentation.

Nanoindentation tests (Agilent Technologies G200, U.S.A. equipped with a Berkovich indentor) at 250 mN with constant loading rate of 0.5 mN/s were also performed, to measure hardness and elastic modulus from loading-unloading curves. The values of hardness and elastic modulus were obtained by averaging 40 indentation tests on transversal cross section at different positions to minimize the effects of sample surface roughness and phase distribution. Room-temperature nano-hardness measurement from Berkovich nano indentation [20] tests is straightforward:

$$H_B = \frac{P}{3\sqrt{3}tan^2(65.27^\circ)\delta_c^2} \cong 0.041\frac{P}{\delta_c^2} \quad (2)$$

Where δ_c is the depth of penetration at the maximum load *(P)*. At the same time, the elastic modulus of the samples *(E)* was calculated from the slope of the unloading curve at maximum load and the projected contact area [20,21]:

$$E = \frac{B}{2\tan 65.27^\circ}\sqrt{\frac{\pi}{3\sqrt{3}}}\frac{S}{\delta_c} \quad (3)$$

where *B* is a geometric factor equal to $B = 1.034$ for a Berkovich indenter [22,23]; *S* is the slope of the load-penetration curve (contact stiffness) computed according to the Oliver-Pharr method [20,23], both are automatically calculated.

Finally the strength of rods in longitudinal direction was measured by flexural tests carried out in a three-point bending test fixture of 10 mm loading span in Instron testing machine (Model 5565 J2634, max. capacity 5 kN, Norwood, MA, USA). In order to measure flexural strength, rods of 1 mm in diameter were fabricated to minimize the presence of the transversal cracks. Six tests were performed at constant crossheads speed of 0.05 mm/min. It was assumed a cylindrical geometry and the flexural strength (σ_f) was calculated according to the expression:

$$\sigma_f = FL/\pi r^3 \quad (4)$$

where *F* is the load applied at the centre of the beam, *L* is the support span (10 mm) and *r* is the radius of the beam. For all experiments the mean value is reported as a result for each material and standard error is actually standard deviation calculated for the total number of tests per material.

3. Results

3.1. Microstructural and crystallographic characterization

In order to obtain better homogeneity in the heating flux around the melt for directional solidification by LFZ, it is normally performed counter-rotating feed rod and pulling crystal. Figure 1 shows a transverse cross-section of a Y_2O_3-MgO eutectic rod grown at 50 mm/h with counter-rotation (50 rpm). The eutectic microstructure consists of MgO fibers (dark phase) embedded in a bright matrix that was detected to be Y_2O_3 (Fig. 1B). Image analysis shows that the solidified rods have the expected amount of MgO, approximately 20 %vol, coincident with the initial composition of the mixtures. The microstructure was not homogeneous and there is a clear evidence of banding by the presence of the coarser Y_2O_3 phase (Fig. 1A). Instabilities in the melt lead to the formation of bands associated to the rotation period as has been also reported before in other eutectic ceramics [24, 25]. A banding periodicity of around 18 μm is measured from longitudinal cross section SEM image (not shown here) which is close to the distance travelled by the rod in a revolution. This indicates that this banding is related to the rotation speed of the rod. Therefore, from now on, all samples have been solidified without rotation with various growth rates to study their effect on microstructural aspects, optical and mechanical properties.

The presence of transverse surface cracks was observed with the naked eye on the eutectic rods grown with final diameter of

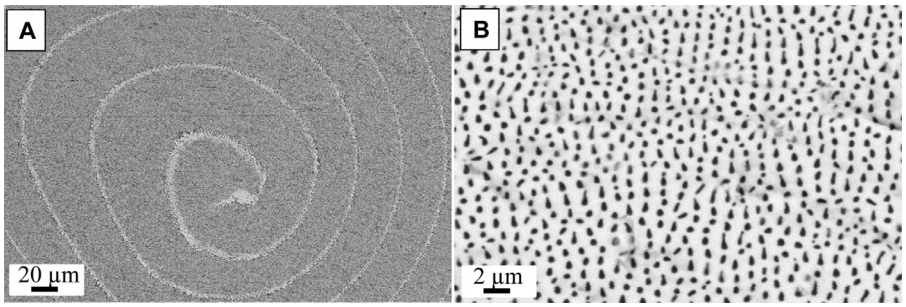

Fig. 1. SEM micrographs of (A) the transverse cross section of MgO-Y2O3 eutectic grown at 50 mm/h with counter-rotation at 50 rpm (Inset shows higher magnification of one banding). (B) Detail of the eutectic microstructure inside banding.

Table 2
Average transverse microstructural features in Y_2O_3-MgO eutectic ceramics grown at various rates by LFZ method. The transverse size has been determined from equivalent rod diameter in equiaxial MgO sections (circular, triangular sections or cell boundaries); or from <width+length>/2 in lamellar section.

Growth rate (mm/h)	Center					Border	
	Interspacing (μm)	Microstructural feature size				Interspacing (μm)	Microstructure feature size
		Fiber	Colony				Fiber
			Volume percentage of cell structure and individual colony size	Intercell	Intracell		
25	1.7±0.2	Circular sec.(0.8±0.05μm)	-	-	-	1.6±0.2	Elliptical sec. (1±0.1μm)
50	1.3±0.1	Almost triangular (0.6±0.02μm) to lamellar (1.5±0.1 μm) Sec.	-	-	-	1.1±0.2	Almost triangular (0.6±0.04 μm) to lamellar sec.(1.4±0.1μm)
100	1.1±0.2	Almost triangular sec.(0.4±0.02μm)	7%-36±5 μm	3.5±0.5μm	Fiber: (0.6±0.05μm) Lamella: (2.5±0.2μm)	0.9±0.1	Almost triangular sec.(0.4±0.02μm)
300	0.6±0.1	-	42%-51±6μm	3.5±0.3μm	Fiber: (0.4±0.03μm) Lamella: (2.2±0.2μm)	0.5±0.05	Almost triangular sec.(0.3±0.01μm)
500	0.5±0.1	-	58%-37±7μm	2.7±0.3μm	Fiber: (0.3±0.05μm) Lamella: (2.4±0.2μm)	0.4±0.05	Almost triangular sec.(0.25±0.05μm)
750	0.4±0.05	-	76%-41±3μm	2.0±0.2μm	Fiber: (0.2±0.04μm) Lamella: (2.5±0.3μm)	0.3±0.04	Almost triangular sec.(0.2±0.06μm)

1.6 mm at any growth rate, whereas those grown with final diameter of 1.0 mm rarely contained transverse cracks and they were considered for further mechanical tests. Although the bonding between both phases was excellent, cracks on the surface may be induced by the high thermal residual stresses developed upon cooling from the processing temperature strongly contributed by the mismatch in thermal expansion coefficients between the MgO and Y_2O_3 phases [4], which was observed in other eutectic systems, too [26,27]. Figure 2 shows representative transverse cross section FE-SEM images of the Y_2O_3-MgO eutectic ceramics grown at different velocities. The microstructural characteristics from analysis of SEM images are listed in Table 2. In the samples solidified with growth rate of 50 mm/h and lower, homogeneous microstructure of MgO fibers parallel to the growth direction embedded in Y_2O_3 matrix was found (Fig. 2 A-D). However, the morphology and the size of MgO fibers changed from 25 mm/h to 50 mm/h. At a growth rate of 25 mm/h, MgO fibers had approximately circular section with 0.8±0.05 μm in diameter in the center of the rod (Fig. 2 A) which mildly changed to elliptical section (equivalent diameter of 1±0.1 μm) in its border (Fig. 2 B) and an eutectic interspacing of 1.6±0.2-1.7±0.2 μm was measured. The higher growth rate of 50 mm/h produced finer MgO fibers and smaller interspacing of 1.3±0.1 and 1.1±0.2 μm in the center and near the border of the grown rod, respectively. Mostly, the fibers presented triangular (0.6±0.02 μm wide) section, elongated, that tend to align in rows (Fig. 2 C), while some evidence of short lamellar section (ribbon-like, 1.5±0.1 μm transverse length) in some areas was also observed (Fig. 2 D). The borders of the mismatch boundaries [28] can also be clearly seen in Fig. 2. Increasing the growth rate to 100 mm/h, there is some evidence of the formation of cells that consisted of only 7 vol% of the grown bar in its center (Fig. 2 E) and it confirms that the solidification suffers a transition from coupled and planar solidification front to cellular regime. For this velocity, the cell size is around 36±5 μm and interspacing decreased to 1.1±0.2-0.9±0.1 μm. The cells presented a boundary formed by coarsened MgO phase of 3.5±0.5 μm. Inside the cell, the microstructure was a rod-like degenerate one, elongating towards the edge of the colony in the transverse cross-section (Fig. 2 E, inset). While 93 vol% of the bar has fine fibrous microstructure with almost triangular section (0.4±0.02 μm) (Fig. 2 E). Another important feature is the presence of grey phase at the cell boundaries. EDS microanalysis showed it

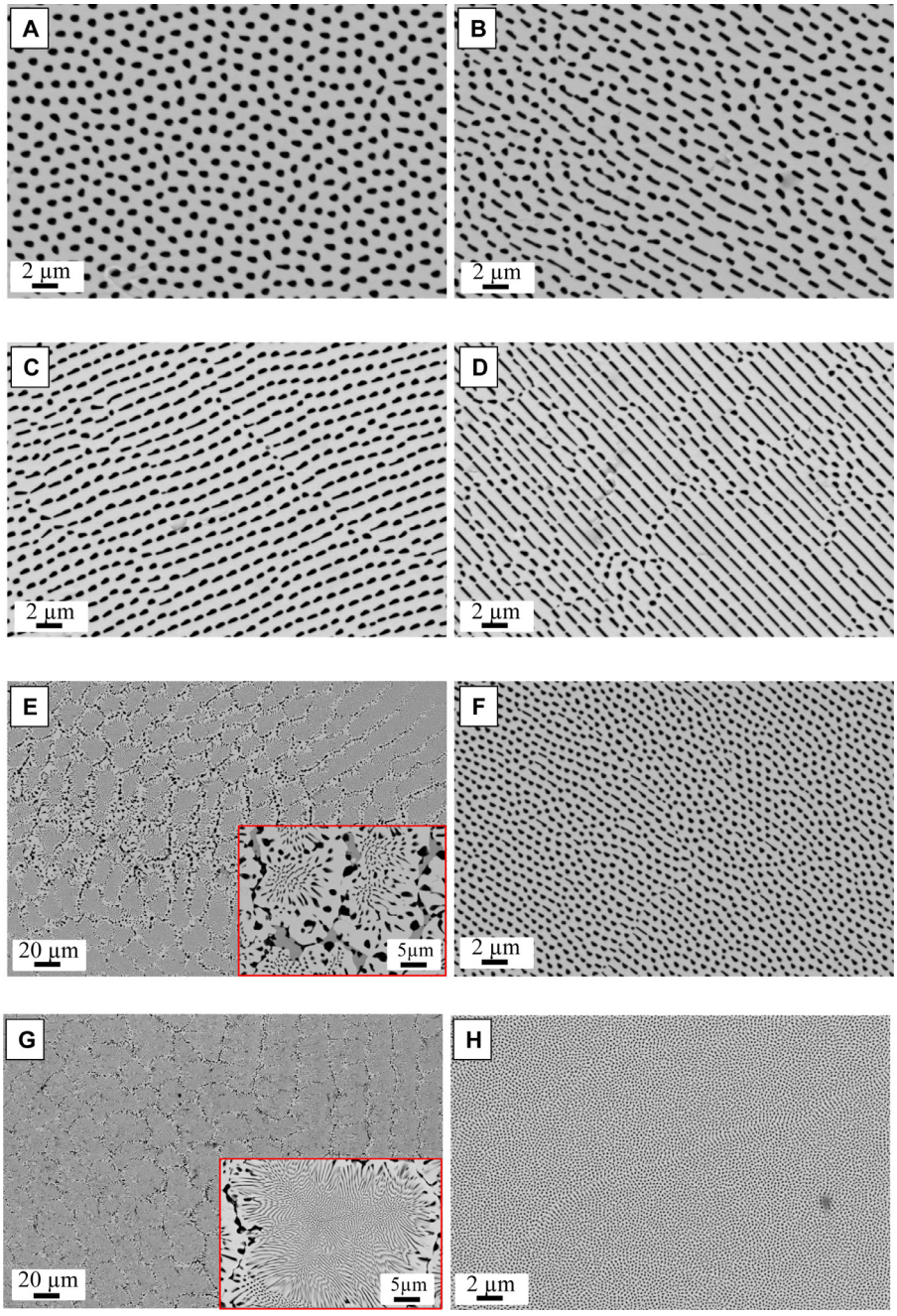

Fig. 2. Transverse cross section SEM images of the Y_2O_3-MgO eutectic ceramics grown at: (A) 25 mm/h in the center, (B) 25 mm/h near the border,(C-D) 50 mm/h in two different areas (E) 100 mm/h in the center, (F) 100 mm/h near the border, (G) 750 mm/h in the center and (H) 750 mm/h near the border. Insets show the microstructure inside the cells. All the eutectic ceramics solidified without rotation.

contains O, Ca, Al, Si and Mg, suggesting it is consequence of the segregation of impurities towards the melt upon solidification.

A similar scenario held for higher growth rates of 300, 500 and 750 mm/h, whereby the cell structure gradually spread and it occupied 76 vol% of the grown bar at 750 mm/h. The microstructural feature size decreased as reported in Table 2 and it showed interspacing values in the range 0.3±0.04-0.4±0.05 µm for the sample solidified at 750 mm/h (Fig. 2 G-H). Furthermore, microstructural evaluation with growth rate was also studied by the interspacing (λ) between MgO phase in the center of the rods as a function of the growth rate (Table 2). The Hunt-Jackson typical quadratic law of $\lambda = cV^{-1/2}$ is fitted to the data, where c is a constant [29] and in this case is equal to 4.8 $\mu m^{3/2}.s^{-1/2}$ (Fig. 3).

XRD diagrams measured as indicated in the experimental section on as grown samples confirm cubic MgO and Y_2O_3 as the phases present in the materials, and are given in Fig. 4. The observed diffraction peaks are compatible with cubic Y_2O_3 ($Ia\bar{3}$, [30] or MgO ($Fm\bar{3}m$, [31]) allowing to estimate approximate lattice parameters of $a = 10.58 \pm 0.02$ Å (1 standard deviation) and $a = 4.23 \pm 0.01$ Å, respectively. Only a few peaks could be seen on each diagram, and often very faint in intensity, which indicates that only a few grains are oriented in the respective plane, that is, there is strong preferential orientation. Some information about the preferential orientation can be obtained from this experiment for the sample solidified at 750 mm/h, that shows strong diffraction peaks corresponding to {222} Y_2O_3 planes. The rest of the

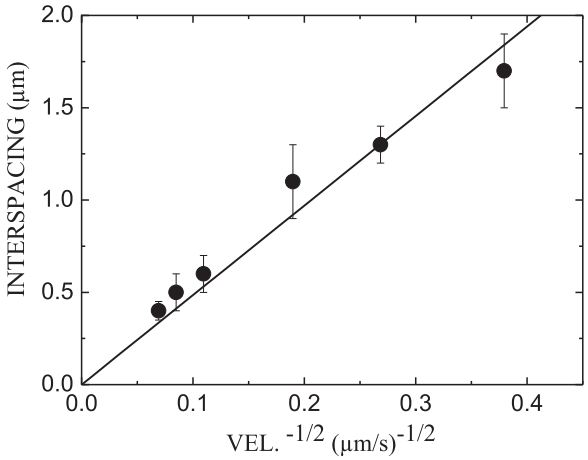

Fig. 3. Inter-spacing versus inverse square root of growth rate for Y_2O_3-MgO eutectic ceramics.

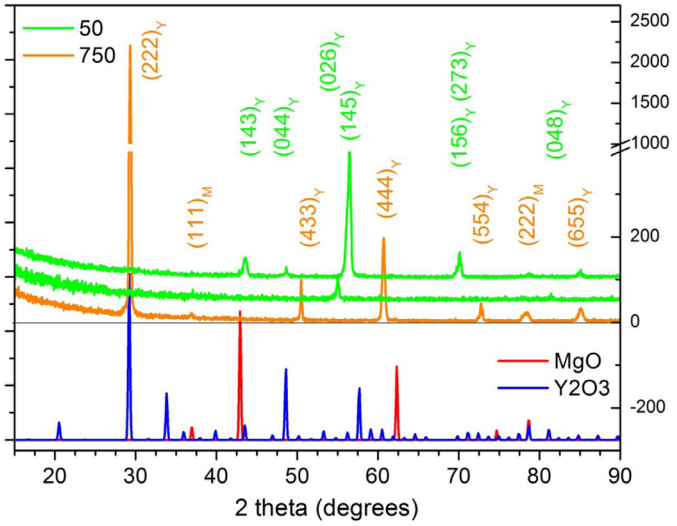

Fig. 4. XRD diagrams of samples as-solidified at 50 mm/h (green lines) and 750 mm/h (orange curve). See text for experimental conditions. The lines are shifted vertically for easy of comparison. In the lower part of the image the theoretical diagrams of MgO (red) and Y_2O_3 (blue) as of references 31 and 30 are given. The diffraction lines are identified with the Miller indices as written on the plot. Subscript M refers to MgO and subscript Y refers to Y_2O_3, with the same color as the diagram where the line is more intense.

peaks are much smaller, and correspond to planes either parallel to this one or they form small angles with it. Small peaks corresponding to {111} and {222} MgO planes can also be seen. One can conclude that in samples with eutectic colonies (uncoupled growth regime) the majority phase Y_2O_3, that leads the solidification, solidifies with <111> directions parallel to the pulling direction. The samples solidified at 50 mm/h (coupled growth regime) show different XRD patterns for each sample, with very low intensity peaks. We did not observe the {222} diffraction peak of Y_2O_3, nor any one near to it. They have certainly preferential orientation, most probably with higher quality (sharper directional distribution) than the samples solidified at large pulling rates. The study of the preferential orientation and orientation relationships between the phases is out of the scope of the present work. Moveover, both component phases are cubic, and thus isotropic from the optical point of view. With respect to the elastic properties the Zener ratio of MgO equals to 1.5 [17], and the one of Y_2O_3 is 1.34 [32], and as a consequence <111> direction, the one that could be clearly identified above, is the stiffest for both components. The respective elastic modulus along this direction are 336 GPa for MgO and 189 GPa for Y_2O_3, to be compared with the average values of corresponding isotropic polycrystalline materials of 310 GPa and 173 GPa respectively [4]. The assumption of isotropic behavior also in elastic properties is expected to be appropriate. As will be seen in the following, one does not need to take into account the preferential orientation of the samples to reach a good comprehension of the material behaviour.

3.2. Mechanical properties

Regarding mechanical properties, Vickers indentation was performed on the transverse section to estimate the hardness and indentation fracture toughness of Y_2O_3-MgO eutectic ceramics grown at variable velocities and the results are listed in Table 3. A mild increase of hardness with the decrease of interspacing was observed, which reaches values up to 11.5±0.3 GPa for eutectic ceramics grown at 750mm/h. The hardness of the grown Y_2O_3-MgO eutectic ceramics is higher than both components of this eutectic as reported values of micro-hardness for Y_2O_3 are ~ 7.6-9 GPa [33, 34] and MgO are about 7–11 GPa [33, 35]. Compared to the well-known 50:50 vol% Y_2O_3-MgO nano-composite with a grain size of ~150-300 nm, different studies have reported optimal Vickers hardness values of 10.5-11.9 GPa [2-4, 7, 10, 11] which agrees with our results (9.7±0.2-11.5±0.3 GPa) in this study, as can be seen in Table 1. It means the hardness is close to that of the 50:50 nano-composite with a lower volume fraction of MgO as a second phase.

Indentation fracture toughness was measured from Vickers imprints for comparison with previous works and the results are displayed in Table 3. A value around 3 MPa.m$^{1/2}$ was obtained for all growth rates, while the indentation fracture toughness of the Y_2O_3 matrix is around 2.0 MPa.m$^{1/2}$ [34]. This fact permits to think that activation of toughening mechanisms by the presence of MgO fibers in the Y_2O_3 matrix takes place. However, indentation fracture toughness of Y_2O_3-MgO eutectic ceramics does not depend strongly on the fiber size and its interspacing. In the case of Y_2O_3-MgO (50:50 vol.%) nanocomposite, the value of 2.5 MPa.m$^{1/2}$ is reported [7].

The measured hardness and elastic modulus by nano-indentor for Y_2O_3-MgO eutectic ceramics grown at variable velocities are listed in Table 3. Higher values of hardness by nano-indentor compared with Vickers for the same rods is a common fact reported before [27], because microindentation imprints are more extended (around 40-45 μm, in our samples) and more sensitive to microstructural defects like pores and micro-cracks which are intrinsically inside the grown rods or created by micro-hardness measurement [27]. However, the displacement into the surface for nanoindentations is around 1000-1200 nm. This means that only sub-micrometric features are subjected to nano-indentation tests. 40 indentation tests on transversal cross section have been performed at different positions to minimize the effects of phase distribution. Mild improvement of hardness with growth rate was also observed which reached to 13.8±2 GPa for eutectic ceramics grown at 750 mm/h. Regarding elastic modulus, the value is ~ 200 GPa independent of solidification rate, although a narrow scatter is unavoidable. This behaviour is expected because the volume fractions of the phases are the same for all growth rates and there are not visible defects, such as voids or microcracks, at the interfaces [17]. This value is comparable with elastic modulus calculated by the rule-of-mixtures model that is a rough approximation of effective elastic modulus of Y_2O_3-MgO eutectic ceramics. With E= 173-180 GPa for Y_2O_3 [4, 36] and E = 310 GPa for MgO [4], the estimated E (assuming the crude way to estimate of elastic modulus by the rule-of-mixtures) for the Y_2O_3-MgO eutectic (80:20 vol%) is

Table 3
Mechanical response by Vickers indentation, nanoindentation and three-point bending tests of Y_2O_3-MgO eutectic ceramics.

Growth rate (mm/h)	Interspacing (μm)		Ave. Vickers indentation for transversal and longitudinal sections 9.81 N (*HV1*)		Nanoindentation for transversal sec. with load of 250 mN (GPa)		Flexural strength (MPa)
	Center	Border	Hardness (GPa)	Toughness (MPa.m$^{1/2}$)	Hardness	Elastic modulus	
25	1.7±0.2	1.6±0.2	9.7±0.2	3.2± 0.8	11.8±2	205±20	203±31
50	1.3±0.1	1.1±0.2	10.2±0.3	3.0± 0.6	12.6±2	213±22	256±25
100	1.1±0.2	0.9±0.1	10.3±0.2	3.0±0.5	12.6±2	204±30	-
300	0.6±0.1	0.5±0.05	10.5±0.2	2.8±0.4	13.1±2	213±17	-
500	0.5±0.1	0.4±0.05	10.8±0.2	2.8±0.5	13.6±2	218±24	-
750	0.4±0.05	0.3±0.04	11.5±0.3	2.9±0.3	13.8±2	224±25	25±6

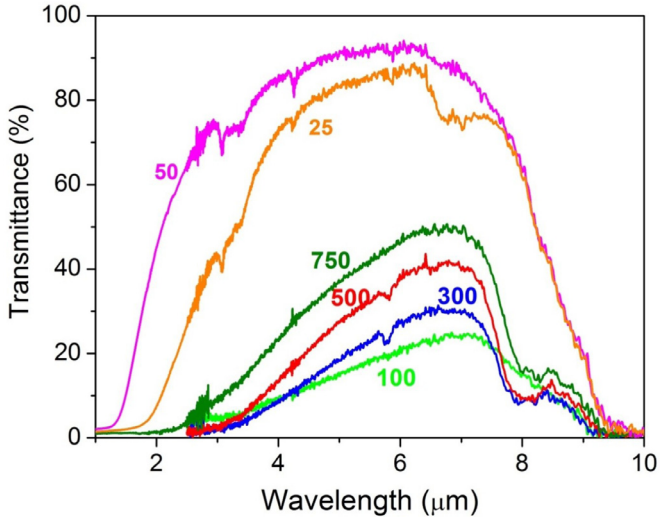

Fig. 5. On axis transmission spectra measured on transverse slices, 1 mm thick, solidified at different pulling rates. The numbers near to the curves indicate the sample pulling rate in mm/h. Line colours (online): orange: 25 mm/h; magenta: 50 mm/h; green: 100 mm/h; blue: 300 mm/h; red: 500 mm/h; olive: 750 mm/h.

200 GPa.Values of 230 GPa have been reported for the Y_2O_3-MgO (50:50 vol %) nanocomposite [4].

Y_2O_3-MgO eutectic rods of around 1 mm in diameter were grown at 25, 50 and 750 mm/h to measure flexure strength at room temperature directly after growing in three-point-bending test and the average values and the corresponding standard errors are listed in Table 3. The actual value of the radius of each grown rod after testing was introduced to the Eq. 4 to calculate flexure strength. An increment of strength with the growth rate from 25 to 50 mm/h was observed, ranging from 203±31 to 256±25 MPa that is expected considering finer MgO fibres and smaller interspacing. At higher growth rate, this tendency failed and it lowered to 25±6 MPa at 750mm/h. This sharp decline is consequence of the cellular microstructure and their coarse boundaries. The maximum obtained strength of 260 MPa at 50 mm/h growth rate is around twofold greater than the value of conventional Y_2O_3 ceramics (120 MPa) [34] and close to those (258-310 MPa) reported for Y_2O_3-MgO (50:50 vol.%) nano-composite [7].

3.3. IR transmission and optical properties

The on-axis optical transmission spectra of 1 mm thick slices cut transverse to the solidification direction as measured with the VIS-NIR and MIR spectrophotometers is given in figure 5. In the experiment, incident light travels mainly along the direction of the microstructure alignment and emerging light propagating in a small cone in this same direction is collected in the detector. To prepare Fig. 5 we have selected, for each sample, the spectra showing the highest measured transmission values from a series of measurements in which the sample was repositioned on the diaphragm. The objective was to select the most homogeneous 0.5 mm diameter region of each sample to measure the transmittance. Other measurements gave transmittance values between 1 and 0.7 times the ones shown in Fig. 5, due to the presence of occasional cracks, inhomogeneous microstructure or local MgO rod alignment divergent from the rod axis.

The transmittance is highest in the central part of the spectra for each sample. Multiphonon absorption processes dominate the long wavelength edge of the spectra. The transparent window for the constituent phases MgO and Y_2O_3 goes to 6.8 and 7.1 μm respectively (absorption coefficient equal to 0.1 cm^{-1}) [37]. At the short wavelength edge, as a consequence of the refractive index contrast between phases in the composite sample, scattering dominates and the material loses transparency. The absorption features around 3 to 3.5 μm, clearly seen in the most transparent samples, can be assigned to OH^- stretching vibrations in the samples, either adsorbed on the surface of as point defects inside MgO or Y_2O_3 [38, 39]. The absorption around 7 μm observed in the sample solidified at 25 mm/h can be associated to residual carbonate species [38]. In fact, absorptions around these wavelengths could be observed in the starting powders (MgO and Y_2O_3) before thermal treatment. To minimize both absorptions in the measured spectra, some slices were heat treated up to 1200 °C with synthetic air flow (< 2ppm H_2O) after polishing, and soon after their transmission spectra measured in the laboratory atmosphere. The spectra shown in Fig. 5 for samples solidified with pulling rates of 25, 50 and 750 mm/h correspond to samples subjected to this thermal treatment. The corresponding absorption features decreased in magnitude, even if they did not disappear completely. On the other hand, the decreased transmittance band at around 8 μm is not affected by the thermal treatment. As it only appears in samples with mainly a colony microstructure, it might be due to phonon absorption of the extra phase found at intercolony areas. Overall, high values of transmittance are observed for light propagating along the alignment of the microstructure in the 4 to 7 μm wavelength range. This is comparable, in transmittance and short wavelength cut-off, to the ones measured by Harris et al. [4] or Xu et al. [8] in 50/50 vol composites with around 150 nm grain size; while the short wavelength cut-off is observed here at longer wavelengths than the values reported by Ma et al [7] or Xie et al. [5].

The transmittance of the sample solidified at 50 mm/h reaches values of 92 % at 6 μm, for a 1 mm thick transverse slice in the spectrum shown. This value is larger than the theoretical maximum for an equivalent homogeneous material with refractive index 1.77 (the volume weighted average refractive index for the composite material using refractive index values given by Stephens [40] and Nigara [41] for MgO and Y_2O_3 respectively). Reflection losses at sharp air-solid interfaces are given by the reflectance R, which for normal incidence at one such surface it is given by $R = |\frac{n-1}{n+1}|^2$, with n being the refractive index of the composite [see for example 4]. At 6 μm R amounts to 7.7 %, so that around 15 % of

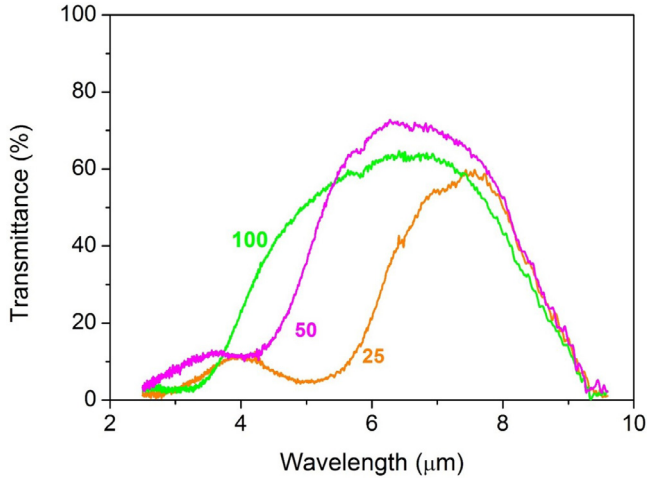

Fig. 6. On axis transmission spectra measured on longitudinal slices, scaled to 1 mm thick, solidified at different pulling rates. The numbers near to the curves indicate the sample pulling rate in mm/h. Line colours (online): orange: 25 mm/h; magenta: 50 mm/h; green: 100 mm/h.

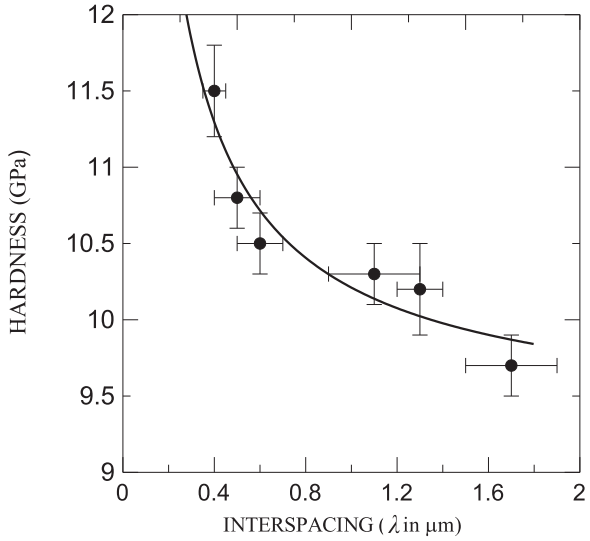

Fig. 7. Vickers hardness from transverse section versus λ for Y_2O_3-MgO eutectic ceramics considered in this study.

the total incident intensity would be reflected in the two surfaces of the slice, and 85% would be the maximum transmittance. Higher transmittance values can be expected for slices coated with broadband antireflective coatings [42]. In the present case, the function of a partial antireflective coating might be imitated by the thermal etching of the surface upon the above mentioned thermal treatment. In fact, observations under the optical microscope suggest a mild corrugation, possibly by selective sublimation of MgO on the surface (or its corrosion reacted product). It is not the purpose of this work to follow further the effect of this surface roughness on the transmittance

The anisotropy of the microstructure warrants exploration of the transmittance also in the direction perpendicular to the solidification direction. The ground and polished longitudinal slices were 0.75 to 0.95 mm thick. For better comparison, the measured transmittance was recalculated to the one corresponding to 1 mm thickness, taking into account the reflectance on the slice surfaces, calculated with Snell equation for normal incidence. That is, the transmittance for a slice of thickness $d_2 = 1$ mm is calculated from the measured transmittance of a slice of thickness d_1 as [4]:

$$T(d_2) \approx (1-R)^2 \left(\frac{T(d_1)}{(1-R)^2} \right)^{d_2/d_1} \quad (5)$$

where R is the reflectance at each surface for normal incidence as written above. n, the refractive index of the slice, was calculated for the composite material as the volume weighted average refractive index at each wavelength. The spectra are shown in Fig. 6, for the materials with homogeneous microstructure, that is, where no colonies were present. Small pieces free from colonies could be found on samples solidified up to 100 mm/h pulling rate. One can observe that the short-wavelength scattering edge shifts towards shorter wavelengths as the microstructure refines, as expected [4]. Compared to the spectra measured in the transverse slices, the attenuation is larger in the longitudinal slices (smaller on axis transmittance). Additionally, there are local transmittance minima at around 5 μm, 4 μm and 2.6 μm, at shorter wavelengths as the microstructure size decreases.

4. Discussion

As observed from the data presented in the previous section, a balance of mechanical and optical transmittance is obtained when the microstructure is both small and homogeneous. Therefore, the highest flexural strength and transmittance values are observed in the samples solidified with the largest pulling rate, while free from colonies. Furthermore, Youngś Modulus of the composite material is around 200 GPa, consistent with the rough approximation of rule-of-mixtures and independent of the microstructure. The measured indentation fracture toughness (IFT) is also independent of the microstructure, and amounts to 3 MPa.m$^{1/2}$, somewhat higher than the IFT of Y_2O_3 ceramics and comparable to values measured for MgO-Y_2O_3 50/50 vol% dense ceramic composites.

The hardness showed however a clear dependence on the microstructural scale which merits some comments. The interspacing (λ, distance between rod centres) dependence of the hardness reasonably fitted into a Hall-Petch (i.e. a $\lambda^{-1/2}$) law and the regression factor was 0.83. This trend is a common fact reported in the literature related to ceramics with respect to grain size [33] and it is based on indentation-induced dislocations pile up at grain boundaries. However, to be honest, hardness can be fitted to any potential law of the type λ^{-p} with $0.5 \leq p \leq 1$ with reasonable accuracy of the same order. It is reported [43], that fitting to a Hall-Petch law has been extensively misused because the assumptions made to derive that law are not satisfied. Indeed, no strong dislocation obstacles and sinks for dislocation motion such as abundant grain boundaries are present here. They analysed these microstructures from a theoretical point of view and they have proposed a general law for the size-effect of the two-phase nature of the eutectic microstructure. Such law follows the general dependence $H \propto Ln\lambda/\lambda$. In the case of the material under study, hardness follows a law which can be displayed as:

$$H = H_0 + 2G\frac{Ln(\lambda/a)}{\lambda/a} \quad (6)$$

where H_0 is the hardness of the monolithic phase, G is its shear modulus and a is the lattice parameter of that phase. We have fitted the experimental values to that equation assuming that only $a \cong 10$ Å is a given parameter (the lattice parameter of Y_2O_3 [44]) and H_0, G are unknown quantities determined by non-linear fitting. Figure 7 shows this calculated curve, which fits to the experimental data satisfactorily with regression factor of 0.90.

From that fitting, these two free parameters are found to be around 9.27 GPa and 67.45 GPa which are close to values of H_0 and G for Y_2O_3 matrix [4, 36] and it validates this equation and the mechanism on which it is based for the hardness dependence of

the Y_2O_3-MgO eutectic. The hardness scales with the mean spacing of the fibers and the fitting to the data is consistent with the well-based law referred to above [43]. A similar analysis in this sense is reported recently in the $MgAl_2O_4$-MgO eutectic since it is shown that MgO fibers in spinel matrix are not as strong as grain boundaries for dislocation blocking and they are not either sinks or sources for them [27]. The same arguments can apply to Y_2O_3-MgO eutectic system with the presence of MgO fibers embedded in Y_2O_3 matrix.

Indentation fracture toughness and flexural strength higher than in single phase Y_2O_3 ceramics indicate that there are strengthening mechanisms operating in the composite. First one has to note that the difference in thermal expansion coefficients (*TEC*) of Y_2O_3 and MgO is large. In the range from 25 °C and 1000 °C, average *TEC* of Y_2O_3 is 9.15 × 10^{-6} K^{-1}, while the one of MgO is around 15.4 × 10^{-6} K^{-1} [4]. This causes high thermoelastic stresses that develop while cooling from the processing temperature, which will be compressive for the matrix Y_2O_3 and tensile for MgO. They can be estimated considering both materials isotropic and defined by their Young Modulus and Poisson ratio (taking from [4]: E_{MgO} = 310 GPa, E_{Y2O3} = 173 GPa, ν_{MgO} = 0.18 and ν_{Y2O3} = 0.3); and assuming a material composed by MgO non-interacting fibers embedded in Y_2O_3 matrix (composite cylinder model [45]). Giving numbers and assuming that stress starts freezing at 1000 °C, one gets for the average hydrostatic component of residual stress at 25 °C, 912 MPa (tensile) in MgO rods and -228 MPa (compressive) in Y_2O_3. The average axial component would be even larger, reaching 1560 MPa tensile stress in MgO or -390 MPa (compressive) in Y_2O_3. Even if the pressure at the interface (of around 590 MPa, the $\sigma_{\theta\theta} = \sigma_{rr}$ components of the residual stress in the MgO fibers calculated with the composite cylinder model) will tend to separate both phases, they kept bonded as solidified (see Fig. 2). The dominant compressive stress in the matrix would strengthen the material, as also suggested in the eutectic composite Al_2O_3-YSZ, where residual stresses are also substantial [24]. Moreover, once the crack starts to propagate it will encounter an inhomogeneous stress field, with fluctuating residual stress with the scale of the microstructure, which will influence its propagation [46].

The evaluation of the fracture surfaces and the path of cracks emanating from the corners of indentation imprints help to understand the interaction of a propagating crack with the microstructure. SEM images of fracture surfaces observed after the bending tests are shown in Fig. 8. As the load increased, cracks started to open in the occasional surface defects of the bar. As a result of the residual stresses (highly tensile in MgO, mildly compressive in the matrix and tensile radial stresses at the interface), MgO fibers or the area near to the interfaces might fail as the crack tip approaches. This and the inhomogeneous stress field in the matrix is ultimately origin of crack deflection, the fracture surface being rougher with features consistent both in size, population, and distribution with the MgO fibers. This observation was more marked for Y_2O_3-MgO eutectic rods grown at 25 and 50 mm/h due to the homogeneous fibrous microstructure (Fig. 8 A and B comparing with C). Fracture tends to occur perpendicularly to the rod axis and frequently small MgO pullouts from the matrix can be seen in the fracture surface. Also, the eutectic grain boundaries (Fig. 8B) can alter cracks propagation along grains with very well aligned microstructure. With eutectic grain boundary we refer to the surface on which two eutectic grains impinge onto each other, so that a break of the crystallographic and microstructural orientations takes place [28].

Figure 9 shows cracks emanating from the corners of the indentation imprints in longitudinal and transverse sections. The cracks present a slightly meandering path across the microstructure. Transgranular (cracks penetrating into the MgO phase) and intergranular (crack deflected near the interfaces) fracture, as well as elastic bridges (Fig. 9 A-B and D) are observed. No clear preference for crack penetration or deflection at the interfaces is evident (Fig. 9 C) [47]. The presence of coarse cell boundaries for a growth rate of 750 mm/h does not decrease indentation fracture toughness even if cracks seem to propagate more easily through them (Fig. 8 C), but causes the material to have much lower strength than the samples with finer, homogenous microstructure. This is completely expected considering the significant change in microstructural characteristics, from fiber size in the scale of ~1 μm for rods grown at 25 and 50mm/h to the cell size of ~40μm for growth rate of 750 mm/h. The finer the microstructure, the smaller the size of the largest preexisting flaw in the composite and the larger its flexural strength value. Similar behavior was observed in other solidified eutectic systems [48].

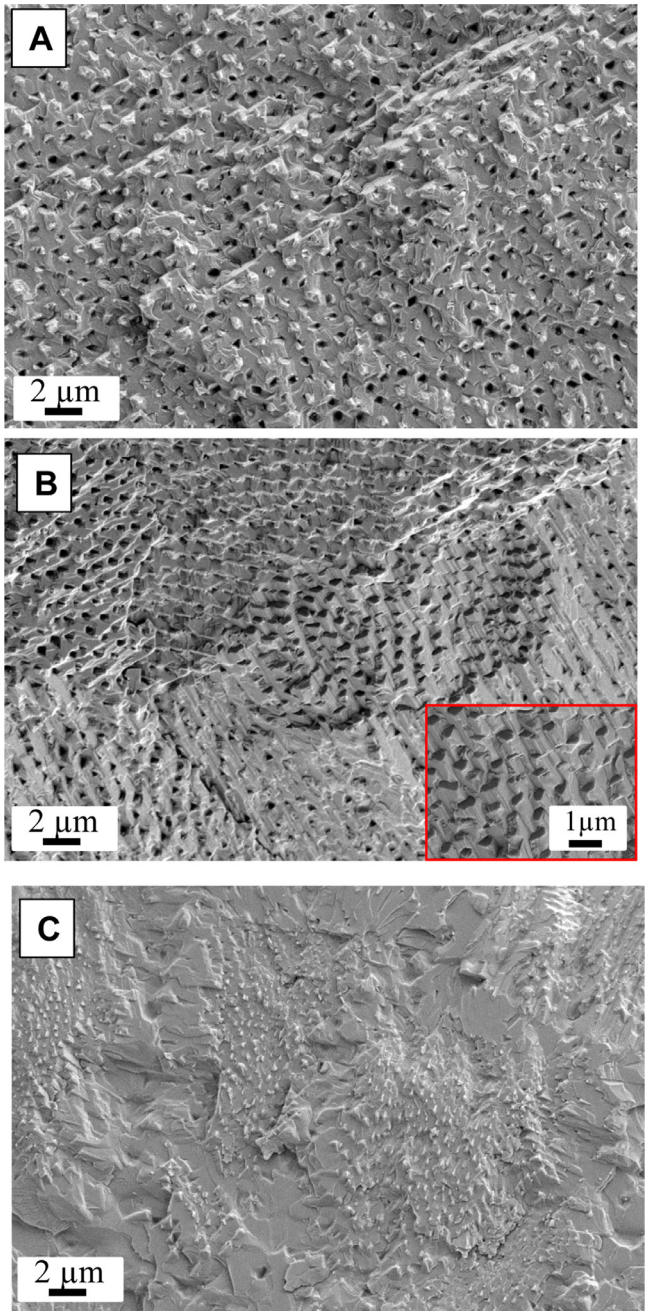

Fig. 8. SEM micrographs offracture surface of Y_2O_3-MgO eutectic ceramics after bending test grown at (A) 25, (B) 50 and (C) 750mm/h after bending testing at room temperature

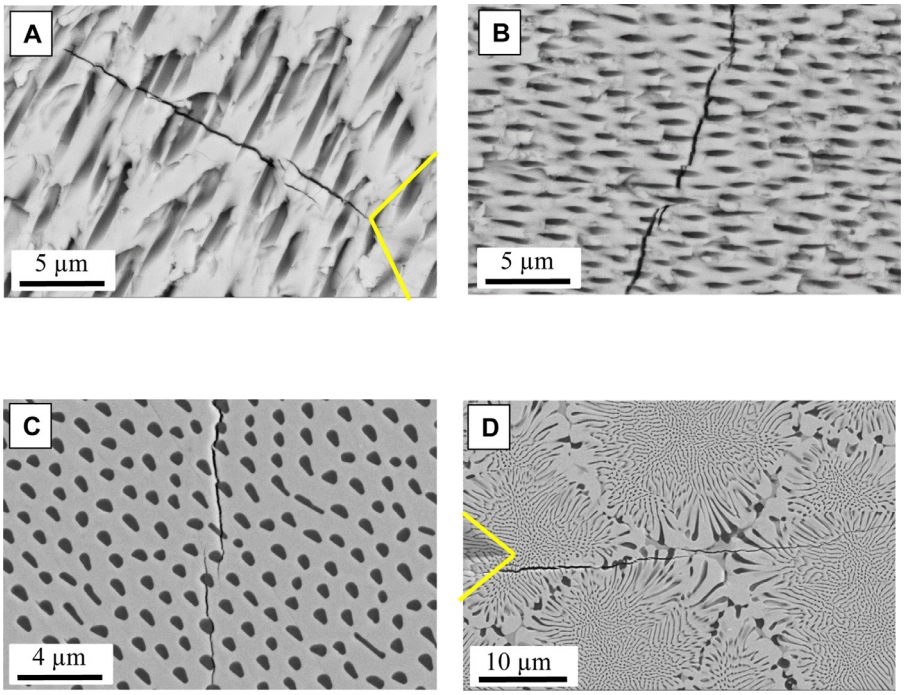

Fig. 9. Crack propagation from a Vickers indentation (indentation marked with yellow), on longitudinal sections of samples solidified at (A) 50 mm/h, (B) 100 mm/h, and on transverse sections of samples solidified at (C) 50 mm/h and (D) 750 mm/h.

As with flexural strength, optical transmittance is also higher for the composites with fine homogenous microstructure. Going from the sample solidified at 25 mm/h to 50 mm/h an increase in transmittance is observed (Fig. 5), concomitant with a decrease in the sample microstructural features. Larger pulling rates start to produce colonies that bring larger microstructural features at their contours, as well as possible third phases, and therefore the scattering is expected to be larger. In consequence, the transmittance of the sample solidified at 100 mm/h is much smaller than the one observed in samples without colonies. With further larger pulling rates, all microstructural features decrease size, and therefore its transmittance increases monotonously again. This scattering behaviour is very similar to the one observed for the eutectic composite MgO-$MgAl_2O_4$ [49], whose microstructure presented similar characteristics. In that case the transmittance extended slightly towards shorter wavelengths because the refractive index contrast was smaller. Additionally, in the spectra for light propagating across the pulling direction there is one local minimum (Fig. 6), whose position also shifts towards shorter wavelengths as the microstructure size decreases. Figure 10 shows, with full black squares, the position of this minimum as a function of the interspacing in the center of the samples (data from Table 2).

A simplified-ideal view of the microstructure of these samples, which solidify in a coupled regime, consists of a triangular arrangement of MgO cylinders (ideally of circular base) inside an Y_2O_3 matrix. The lattice parameter of this 2D arrangement can then be identified with the interspacing determined from SEM images, as given in Table 2. From the optical point of view such a structure is expected to scatter light, with forbidden propagation along some directions and wavelengths. In the wavelength region of interest, the refractive index contrast is $n_{rod}/n_{matrix} = 0.89$ (at wavelength of 4 μm), with a matrix refractive index of 1.84 and it has filling fraction $f = 0.20$ (or radius of cylinder/ lattice parameter = 0.23) [40, 41]. The contrast is not enough to expect a complete gap, according to the gap recipe given by Joannopoulos et al. [50], which state one requires a minimum of index contrast of around 1.4 for a full gap. Instead, only hindered propagation in some directions could be reasonably expected. Gaps could open, if any, at the edge of the Brillouin zone of the photonic lattice. Sakoda [Figure 4.5 in 51] reports for example hindered propagation along the Γ-*M* direction in both polarizations (Electric field or Magnetic field parallel to the low index rods, *E*-pol or *H*-pol respectively) for the case of $n_{high}/n_{low} = 1.65$ and $f = 0.65$. The broadest gap is the first one, appearing in the upper side of the first band. No full gap was predicted for Γ-*K* propagation (see for example figure 3.7 of the same reference). With this reference in mind, we turn to our case and

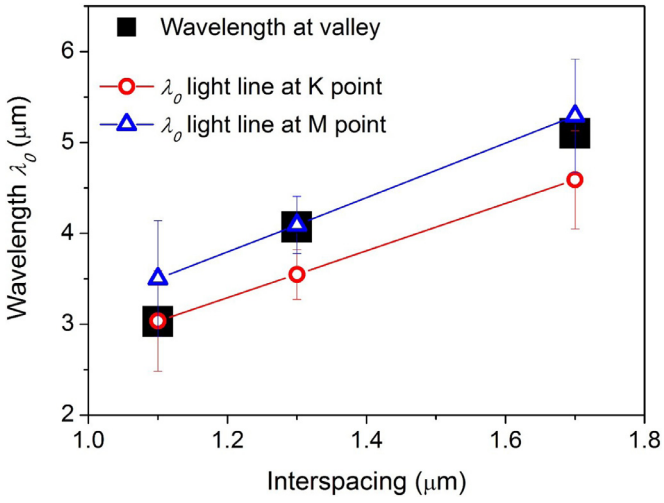

Fig. 10. Wavelength of the local minima in the transmission spectra of longitudinal slices as a function of interspacing of the microstructure (full black squares). The light line wavelength at *K* and *M* points of the first band of a reciprocal lattice of a *2D* triangular arrangement of MgO rods into Y_2O_3 with the lattice parameter equal to the interspacing and 0.20 filling ratio are plotted with open symbols (red circles, *K* point) (blue triangles, *M* point). The error bars correspond to the error bars given in Table 1 for the interspacing. The lines are guides to the eye. (See text for details).

consider that, given the small contrast, the effective refractive index is going to be very similar for both polarizations (*E*-pol or *H*-pol). Let us then take a common averaged refractive index as the volume averaged refractive index, $<n>$. The light line is given by:

$$w = c_0 k / < n >= (2pc_0/l_0) \quad (7)$$

where k is the wave-vector, c_0 is the light velocity in vacuum, and λ_0 is the wavelength in vacuum. In the model *2D* lattice, *M* and *K* points of the reciprocal lattice appear at the lattice wavevectors:

$$k_K = (4p)/(3a_0) \text{ and } k_M = (2p)/(a_0\sqrt{3}) \quad (8)$$

being a_0 the lattice parameter of the microstructure. Using the literature values for the refractive index and as lattice parameter the interspacing values given in Table 2 and Eqs 7 and 8, one easily obtains the light wavelength (λ_0) for propagation vectors (k) at the *K* and *M* points of the first Brillouin zone. Those values are also plotted in Fig. 10 with open symbols. As the refractive index changes smoothly in the wavelength range of interest, the dependence with the lattice parameter is approximately linear. Convincingly enough, the experimental local minima in the on-axis transmittance spectra coincide with the wavelength at *M* point. The deviation of the point corresponding to the 100 mm/h sample might well be related to the larger uncertainty of this experimental value (see Fig. 6).

As the light wavelength approaches the edge of the reciprocal photonic lattice (first Brillouin zone), scattering increases and on-axis transmission decreases. In the present case, the scattering decreases again once the propagation wavenumber surpasses the edge of the first Brillouin zone and transmittance recovers partially. In a perfectly ordered lattice, this would imply again total transmittance. But the material under study is far from being completely ordered. On the one side the microstructure is not perfectly periodic, but more of a glassy-like nature with short-range well defined order and loss of large distance ordering. On the other side, the material consists of different eutectic grains, with different microstructural orientations, and thus incoming light propagates in different photonic lattice directions in each eutectic grain. Whether light with frequency $(c_0 k_K)/2\pi <n>$ is hindered of propagation inside the material to a large extent (at large solid angle of propagation inside the *2D* plane) or not, cannot be told by the present experiments, as it is not possible to identify other possible frequencies with hindered propagation at higher energy (disorder surviving pseudo-gaps). Would it be the case, a high temperature material with light propagation control would be available. This will be the subject of future work.

To end this section, we want to comment on the limitations and possible extension of the material preparation procedure. First of all, a glance at Table 1, where data for the present material solidified at 50 mm/h are included in the last row, shows that performance parameters (mechanical or optical) are competitive with the ceramic nanocomposites found in the literature. In order to get samples free of cracks, in the present case we had to limit ourselves to low diameter rods (1 mm). This is required to prevent cracking associated to the large thermal gradient at the solidification front and growing crystal inherent to the laser floating zone method. Other solidification techniques with smaller solidification gradients would overcome this size limitation, as for example Bridgman [13] or by after-heating the solidifying crystal. However, decreasing thermal gradients at the solidification interface also requires lower solidification rates in order to keep the eutectic solidification in the coupled regime and avoid colony formation. Coarser microstructures would be achieved with the concomitant shift of the scattering cut-off towards longer wavelengths and decrease of the flexural strength. A compromise should be achieved, depending on the intended application. When directionality of the microstructure (and its associated optical behavior) is not required, other solidification techniques could be used to generate extended areas with coupled, small sized homogeneous microstructure. These are for example the techniques relying on laser selective melting [52, 53, 54] with appropriate control of the processing thermal residual stresses. It is to be taken into account that the large difference of TECs between components of this composite might pose strong requirements to these procedures.

As for the optical transparency in the NIR, the larger microstructural size of the solidified materials with homogeneous microstructure (see Table 2) when compared to the nanocomposites found in the literature (Table 1), gives as a result that the solidified material outperforms the nanoceramics only when light propagates along the solidification direction, or whenever anisotropy in light propagation is required. Upon these instances, even the small diameter rods produced by the laser floating zone method, with their observed anisotropy of light propagation, may have application slots such as in infrared emissivity control or as small infrared windows.

5. Conclusions

The preceding results provide answer to the questions posed in the introduction about the material under study. Y_2O_3-MgO composites with eutectic composition (20 % vol MgO) have been effectively solidified from the melt using the laser floating zone method. The material solidifies coupled, and thus generates a dense composite with homogeneous microstructure of MgO rods embedded in Y_2O_3 matrix at pulling rates up to 50 mm/h. From 100 mm/h upwards the microstructure consists of eutectic cells. The highest 3-point flexural strength values and highest MIR optical transmittance has been observed for the material solidified with the finest, still homogeneous microstructure. Flexural strength is comparable to the values found in literature for dense ceramic nanocomposites with 50/50 vol% composition, as well as indentation fracture toughness. MgO rod dispersion and the associated residual thermal stresses contribute to strengthen the material, as they place the Y_2O_3 matrix under residual compressive stress and deviate the propagating crack increasing the fracture energy. The infrared transmittance is also comparable, with large transmittance values for the material solidified at 50 mm/h when light propagates along de solidification direction, but which do not match the transmittance level of some of the values found in literature for the finest and denser achieved composites. Still, the alignment of the microstructure induces optical effects in the infrared range of photonic crystal nature for light propagating perpendicular to the solidification direction that could allow applications not possible for the isotropic bimaterial composites being optimized by the advanced sintering procedures.

Declaration of Competing Interest

The authors declare that they have no known competing financial interests or personal relationships that could have appeared to influence the work reported in this paper.

Acknowledgements

This work was supported by the Ministerio de Economía y Competitividad (Government of Spain) and FEDER Funds under Grants No. MAT77769-R and Gobierno de Aragón, Subvención a Grupos de Investigación No. T02_20R. BMM wants to acknowledge the support of the Spanish MINECO by means of a “Juan de la Cierva-Incorporación” fellowship during her sabbatical stay in Zaragoza and is grateful to the Ministerio de Economía y Competitividad for the research funding through the project PID2019-103847RJ-I00 and ‘Junta de Andalucía’ through the project P18-RTJ-1972. We

want to thank Rubén Gotor for his help in several tasks of material preparation. Authors would like to acknowledge also the use of the Servicio General de Apoyo a la Investigación SAI, Universidad de Zaragoza, namely, the Service of Electron Microscopy of Materials and the Service of X-ray Diffraction and Fluorescence Analysis.

References

[1] Ch. Barad, G. Kimmel, D. Shamir, K. Hirshberg, Y. Gelbstein, Lattice variations in nanocrystalline Y_2O_3 confined in magnesia (MgO) matrix, J Alloys Comp 801 (2019) 375–380.
[2] H. Sun, Y. Zhang, H. Gong, T. Li, Q. Li, Microwave sintering and kinetic analysis of Y_2O_3-MgO composites, Ceram. Int. 40 (2014) 10211–10215.
[3] J. Wang, D. Chen, E.H. Jordan, M. Gell, Infrared-transparent Y_2O_3-MgO nanocomposites using sol-gel combustion synthesized powder, J. Am. Ceram. Soc. 93 (2010) 3535–3538.
[4] D.C. Harris, L.R. Cambrea, L.F. Johnson, R.T. Seaver, M. Baronowski, R. Gentilman, C.S. Nordahl, T. Gattuso, S. Silberstein, P. Rogan, Th. Hartnett, B. Zelinski, W. Sunne, E. Fest, H. Poisl, Ch.B. Willingham, G. Turri, C. Warren, M. Bass, D.E. Zelmon, S.M. Goodrich, Properties of an infrared-transparent MgO:Y_2O_3 nanocomposites, J. Am. Ceram Soc. 96 (2013) 3828 -385.
[5] J. Xie, X. Mao, Q. Zhu, B. Jiang, L. Zhang, Influence of synthesis conditions on the properties of Y_2O_3-MgO nanopowders and sintering nanocomposites, J. Eur. Ceram Soc. 37 (2017) 4095–4101.
[6] Sh. Xu, J. Li, Ch. Li, Y. Pan, J. Guo, Hot pressing of infrared-transparent Y_2O_3-MgO nanocomposites using sol-gel combustion synthesized powders, J. Am. Ceram Soc. 98 (2015) 1019–1026.
[7] H.J. Ma, W.K. Jung, Ch. Baek, D.K. Kim, Influence of microstructure control on optical and mechanical properties of infrared transparent Y_2O_3-MgO nanocomposite, J. Eur. Ceram Soc. 37 (2017) 4902–4911.
[8] Sh. Xu, J. Li, H. Kou, Y. Shi, Y. Pan, J. Guo, Spark plasma sintering of Y_2O_3–MgO composite nanopowder synthesized by the esterification sol–gel route, Ceram. Int. 41 (2015) 3312–3317.
[9] D.T. Jiang, A.K. Mukherjee, Spark plasma sintering of an infrared-transparent Y_2O_3-MgO nanocomposite, J. Am. Ceram Soc. 93 (2010) 769–773.
[10] D.A. Permin, M.S. Boldin, A.V. Belyaev, S.S. Balabanov, A.V. Novikova, V.A. Koshkin, A.A. Murashov, I.V. Ladenkov, A.A. Popov, E.A. Lantsev, N.M. Khamaletdinova, IR-transparent MgO-Y_2O_3 ceramics by self-propagating high-temperature synthesis and spark plasma sintering, Ceram. Int. 46 (2020) 15786–15792.
[11] L. Liu, K. Morita, T.S. Suzuki, B.N. Kim, Effect of volume ratio on optical and mechanical properties of Y_2O_3-MgO composites fabricated by spark-plasma-sintering process, J. Eur. Ceram. Soc. 41 (2021) 2096–2105.
[12] S.G. Tresvyatskii, L.M. Lopato, A.A. Ogorodnikova, A.V. Shevchenko, Phase diagrams of systems formed by yttrium, erbium, and ytterbium oxides with magnesium oxide, Inorg. Mater. 7 (1971) 1798–1801.
[13] J. LLorca, V.M. Orera, Directionally solidified eutectic ceramic oxides, Prog. Mater. Sci. 51 (2006) 711–809.
[14] V.S. Stubican, R.C. Bradt, Eutectic solidification in ceramic systems, Annu. Rev. Mater. Sci. 11 (1981) 267–297.
[15] C. Rode, T. Bunch-Nielsen, K.K. Hansen, B. Grelk, Moisture damage with magnesium oxide boards in Danish façade structures, Energy. Proc. 132 (2017) 765–770.
[16] V.M. Orera, J.I. Peña, Directional solidification", pages 417-457, in: By N.P. Bansal, A.R. Boccaccini (Eds.), Ceramics and Composites Processing Methods, The American Ceramic Society, John Wiley and Sons Inc, 2012 Diagrams showing the procedure are presented in figures 12.6 and 12.7.
[17] D.J. Green, An introduction to the mechanical properties of ceramics, Cambridge University Press, Cambridge, UK, 1998.
[18] G.R. Anstis, P. Chantikul, D.B. Marshall, B.R. Lawn, A critical evaluation of indentation techniques for measuring fracture toughness: I direct crack measurements, J. Am. Ceram. Soc. 64 (1981) 533–538.
[19] K.M. Liang, G. Orange, G. Fantozzi, Evaluation by indentation of fracture toughness of ceramic materials, J. Mater. Sci. 25 (1990) 207–214.
[20] A.C. Fischer-Cripps, Nanoindentation, Springer, New York, New York, NY, 2004.
[21] E. Broitman, Indentation hardness measurements at macro-, micro-, and nanoscale: a critical overview, Tribol. Lett. 65 (2017) 23.
[22] W.C. Oliver, G.M. Pharr, An improved technique for determining hardness and elastic modulus using load and displacement sensing indentation experiments, J. Mater. Res. 7 (1992) 1564–1583.
[23] W.C. Oliver, G.M. Pharr, Measurement of hardness and elastic modulus by instrumented indentation: advances in understanding and refinements to methodology, J. Mater. Res. 19 (2004) 3–20.
[24] J. Llorca, J.Y. Pastor, P. Poza, J.I. Peña, I. de Francisco, A. Larrea, V.M. Orera, Influence of the Y_2O_3 content and temperature on the mechanical properties of melt-grown Al_2O_3-ZrO_2 eutectics, J. Am. Ceram. Soc. 87 (2004) 633–639.
[25] D. Sola, P.B. Oliete, R.I. Merino, J.I. Peña, Directionally solidified Ni doped MgO-MgSZ eutectic composites for thermophotovoltaic devices, J. Eur. Ceram Soc. 39 (2019) 1206–1213.
[26] F.L. Kennard, R.C. Bradt, V.S. Stubican, Eutectic solidification of MgO-$MgAl_2O_4$, J. Am. Ceram. Soc. 56 (1973) 566–569.
[27] B.M. Moshtaghioun, J.I. Peña, Non-Hall-Petch hardness dependence in ultrafine fibrous MgO-$MgAl_2O_4$ eutectic ceramics fabricated by the laser-heated floating zone (LFZ) method, J. Eur. Ceram Soc. 39 (2019) 3208–3212.
[28] L.M. Hogan, R.W. Kraft, F.D. Lemkey, Eutectic Grains, in: H. Herman (Ed.), Advances in Materials Reserch 5, John Wiley & Sons Inc, New York, 1971.
[29] K.A. Jackson, J.D. Hunt, Lamellar and rod eutectic growth, Trans. Metal. Soc. AIME. 236 (1966) 1129–1142.
[30] Inorganic Crystal Structure Database (ICSD), collection code number 52026 from Q. Lu, Q. Yang, S. Lu, C. Jiang, Fabrication, structure refinement, and EXAFS analysis of yttrium lanthanum oxide transparent ceramics, Optical Materials 36 (2014) 1289–1294.
[31] Inorganic Crystal Structure Database (ICSD), collection code number 193042 from V.G. Tsirelson, A.S. Avilov, Yu.A. Abramov, E.L. Belokoneva, R. Kitaneh, D. Feil, X-ray and electron diffraction study of MgO, Acta Crystallographica, Section B: Structural Science 54 (1998) 8–17.
[32] A. Sayir, J. W. Palko, W.M. Kriven, S. V. Sinogeikin and J. D. Bass, Single-Crystal Elastic Constants of Yttria (Y2O3) Measured to High Temperatures, NASA Technical Report Server, document ID: 20050201648. https://ntrs.nasa.gov/citations/20050201648 (accessed: 12th November 2019).
[33] R.W. Rice, C.C. Wu, F. Borchelt, Hardness-grain size relation in ceramics, J. Am. Ceram. Soc. 77 (1994) 2539–2553.
[34] B. Ahmadi, Sh.Razavi Reza, M. Ahsanzadeh-Vadeqani, M. Barekat, Mechanical and optical properties of spark plasma sintered transparent Y_2O_3 ceramics, Ceram. Int. 42 (2016) 17081–17088.
[35] D.Y. Chen, E.H. Jordan, M. Gell, Pressureless sintering of translucent MgO ceramics, Scr. Mater. 59 (2008) 757–759.
[36] O. Yeheskel, O. Tevet, Elastic moduli of transparent yttria, J. Am. Ceram. Soc. 82 (1999) 136–144.
[37] W.J. Tropf, M.E. Thomas, T.J. Harris, Properties of Crystals and Glasses, p 33.3, in: M. Bass (Ed.), Handbook of Optics: Devices, measurements and Properties, Vol II, 2nd ed., Mc Graw-Hill, Inc, 1995.
[38] M. Ivanov, E. Kalinina, Yu Kopylov, V. Kravchenko, I. Krutikova, U. Kynast, Jiang Li, M. Leznina, A. Medvedev, Highly transparent Yb-doped $(La_xY_{1-x})_2O_3$ ceramics prepared through colloidal methods of nanoparticles compaction, J. Europ. Ceram. Soc 36 (2016) 4251–4259.
[39] G.C. Wei, Extrinsic OH^- absorption in Transparent Polycrystalline lanthana–Doped Yttria, J. Am. Ceram Soc. 71 (1988) C20–C23.
[40] R.E. Stephens, I.H. Malitson, Index of Refraction of Magnesium Oxide, J. Nat. Bur. Stand. 49 (1952) 249–252.
[41] Y. Nigara, Measurement of the Optical Constants of Yttrium Oxide, Jpn. J. Appl. Phys. 7 (1968) 404–408.
[42] H.K. Raut, V.A. Ganesh, A.S. Nairb, S. Ramakrishna, Anti-reflective coatings: a critical, in-depth review, Energy Environ. Sci. 4 (2011) 3779–3804.
[43] Y. Li, A.J. Bushby, D.J. Dunstan, The Hall–Petch effect as a manifestation of the general size effect, Proc. R. Soc. A472 (2016) 20150890.
[44] Y.N. Xu, Z. Gu, W.Y. Ching, Electronic, structural, and optical properties of crystalline yttria, Phys. Rev. B 56 (1997) 14993–15000.
[45] B. Budiansky, J.W. Hutchinson, A.G. Evans, Matrix fracture in fiber-reinforced ceramics, J. Mech. Phys. Solids 34 (1986) 168–189.
[46] L. Perrière, R. Valle, N. Carrère, G. Gouadec, Ph. Colomban, S. Lartigue-Korinek, L. Mazerolles, M. Parlier, Crack propagation and stress distribution in binary and ternary directionally solidified eutectic ceramics, J. Europ. Ceram. Soc. 31 (2011) 1199–1210.
[47] M.Y. He, A.G. Evans, J.W. Hutchinson, Crack deflection at an interface between dissimilar elastic materials: role of residual stresses, Int. J. Solid Structures 31 (1994) 3443–3455.
[48] J.Y. Pastor JY, J. LLorca, P. Poza, I de Francisco, R.I. Merino, J.I. Peña, Mechanical properties of melt-grown Al_2O_3-ZrO_2(Y_2O_3) eutectics with different microstructure, J Eur. Ceram Soc 25 (2005) 1215–1223.
[49] B.M. Moshtaghioun, J.I. Peña, R.I. Merino, Medium infrared transparency of MgO-$MgAl_2O_4$ directionally solidified eutectics, J. Europ. Ceram. Soc. 40 (2020) 1703–1708.
[50] J.D. Joannopoulos, S.G. Jonhnosn, J.N. Winn, R.D. Meade, Photonic Crystals: Molding the Flow of Light, 2nd Edition, Princeton University Press, Princeton and Oxford, 2008.
[51] K. Sakoda, Optical Properties of Photonic Crystals, Springer-Verlag, Berlin, 2001.
[52] J. Gurauskis, V. Lennikov, G.F. de la Fuente, R.I. Merino, Laser-assisted, crack--free surface melting of large eutectic ceramic bodies, J. Europ. Ceram. Soc. 31 (2011) 1251–1256.
[53] J. Wilkes, Y.C. Hagedorn, W. Meiners, K. Wissenbach, Additive manufacturing of ZrO_2-Al_2O_3 ceramic components by selective laser melting, Rapid prototyping Journal 19 (2013) 51–57.
[54] Z. Fan, Y. Zhao, Q. Tan, N. Mo, M.X. Zhang, M. Lu, H. Huang, Nanostructured Al_2O_3-YAG-ZrO_2 ternary eutectic components prepared by laser engineered net shaping, Acta Mater. 170 (2019) 24–37.